The Astrophysical Journal, 697:68–78, 2009 May 20 doi:10.1088/0004-637X/697/1/68

DENSITY-ENHANCED GAS AND DUST SHELLS IN A NEW CHEMICAL MODEL FOR IRC+10216

M. A. Cordiner[1] and T. J. Millar
Astrophysics Research Centre, School of Mathematics and Physics, Queen's University, Belfast BT7 1NN, UK; m.cordiner@qub.ac.uk
Received 2008 September 15; accepted 2009 March 4; published 2009 April 30

ABSTRACT

A new chemical model is presented for the carbon-rich circumstellar envelope (CSE) of the asymptotic giant branch star IRC+10216. The model includes shells of matter with densities that are enhanced relative to the surrounding circumstellar medium. The chemical model uses an updated reaction network including reactions from the RATE06 database and a more detailed anion chemistry. In particular, new mechanisms are considered for the formation of CN^-, C_3N^-, and C_2H^-, and for the reactions of hydrocarbon anions with atomic nitrogen and with the most abundant cations in the CSE. New reactions involving H^- are included which result in the production of significant amounts of C_2H^- and CN^- in the inner envelope. The calculated radial molecular abundance profiles for the hydrocarbons C_2H, C_4H, and C_6H and the cyanopolyynes HC_3N and HC_5N show narrow peaks which are in better agreement with observations than previous models. Thus, the narrow rings observed in molecular microwave emission surrounding IRC+10216 are interpreted as arising in regions of the envelope where the gas and dust densities are greater than the surrounding circumstellar medium. Our models show that CN^- and C_2H^- may be detectable in IRC+10216 despite the very low theorized radiative electron attachment rates of their parent neutral species. We also show that magnesium isocyanide (MgNC) can be formed in the outer envelope through radiative association involving Mg^+ and the cyanopolyyne species.

Key words: astrochemistry – circumstellar matter – ISM: molecules – stars: individual (IRC+10216)

Online-only material: color figures

1. INTRODUCTION

The carbon-rich asymptotic giant branch (AGB) star IRC+10216 is among the richest known sources of molecules in the sky. The star is nearing the end of its life and is rapidly losing mass to the interstellar medium. Over 60 species have been detected in the expanding circumstellar envelope (CSE), which extends more than 10,000 AU from the star. The outflow from the central star is carbon-rich (with [C]/[O] > 1), and contains abundant stable molecules such as C_2H_2, HCN, and CH_4, which are formed in the hot inner regions near the stellar surface (Lafont et al. 1982). As the density falls with radius, interstellar ultraviolet (UV) photons penetrate the CSE and cause the photolysis of these "parent" molecules. This results in the production of reactive species that subsequently participate in a complex gas-phase chemistry to produce new "daughter" molecules in the outer envelope. Chemical models of this environment (see Millar et al. 2000, for example) are able to reproduce with good accuracy the observed column densities of outer-envelope species such as the carbon chains C_nH (for $n = 2, 4, 6, 8$). However, it has been suggested that such chemical models are inconsistent with observed C_nH rotational emission maps (see, for example, Guélin et al. 1999). The observations show C_nH emission maxima at around the same radius (for different n), whereas the results of chemical models show spatially separated peak abundances. The modeled molecular radial distributions are also broader than observed. Using optical imaging, Mauron & Huggins (2000) detected multiple dust shells in the envelope of IRC+10216, spaced at regular intervals of ∼5″–20″. These shells were interpreted as arising as a result of modulation of the stellar mass-loss rate, perhaps due to the presence of a binary stellar companion. Brown & Millar (2003) included density-enhanced circumstellar dust shells in their chemical model for IRC+10216 in an attempt to make the model more physically realistic and to address the discrepancies between observed molecular emission maps and the results of previous chemical models. The addition of dust shells modifies the radiation field inside the CSE and results in modeled molecular abundance profiles that are in better agreement with the observations.

Figure 1 shows the effect of the Brown & Millar (2003) density-enhanced dust shells on the modeled C_2H, C_4H, and C_6H radial profiles in IRC+10216. In the presence of dust shells, the molecular abundance peaks move outward and slightly closer together. The C_2H profile full width at half-maximum narrows from 7″ to 6″ and moves from 8″ to 18″. According to Guélin et al. (1999), the molecular emission maps from C_2H, C_4H, and C_6H all peak in a narrow circumstellar ring about 2″ wide at a radius about 15″ from the star. It is therefore clear that although the radial distributions of the species in Brown & Millar's (2003) model represent a better match than previous models, they are still too broad to fully explain the observed maps. In addition, C_6H peaks at a larger radius than C_2H and C_4H, which is inconsistent with the observations.

Dinh-V-Trung & Lim (2008) mapped the molecular shells of HC_3N and HC_5N in IRC+10216 at unprecedented angular resolution. The shells were found to be clumpy, co-spatial with each other and with a structure closely matching the distribution of dust shells observed by Mauron & Huggins (2000). It was concluded that the circumstellar cyanopolyyne gas density distribution matches that of the dust and therefore that the gas and dust are coupled. Shell-like structures ∼2″ wide are present in the maps of Dinh-V-Trung & Lim (2008), which are inconsistent with the ∼10″ wide abundance profiles calculated in the model of Brown & Millar (2003).

In this article, a new chemical model for IRC+10216 is presented which builds on previous models and includes density-

[1] Contact Address: Solar System Exploration Division, Mailstop 690.3, NASA Goddard Space Flight Center, Greenbelt, MD 20771, USA.

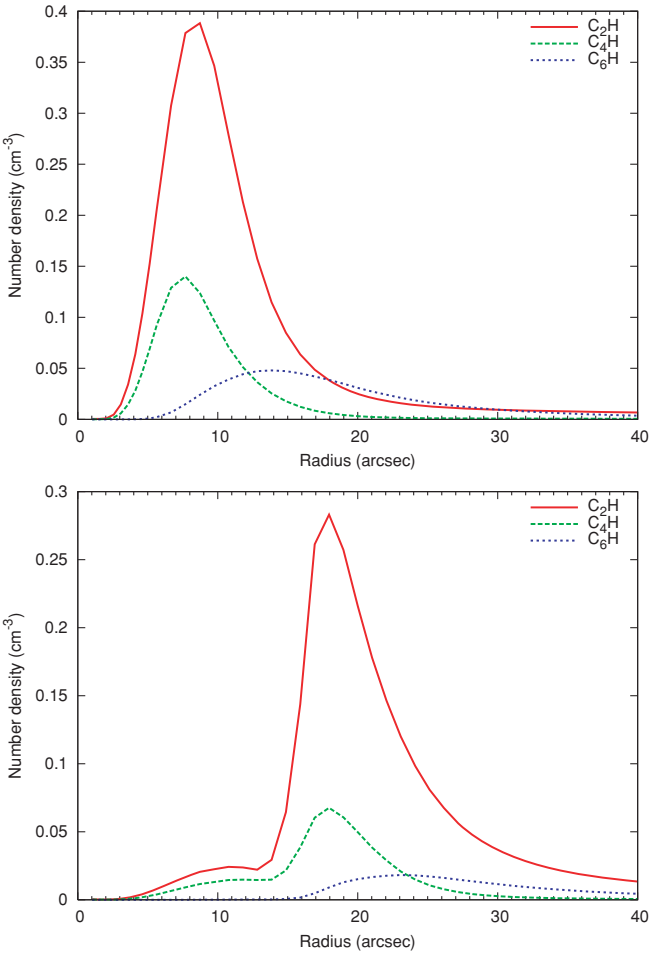

Figure 1. Radial molecular abundance profiles for C_2H, C_4H, and C_6H in IRC+10216, calculated in a model with no density-enhanced shells (top), and with the density-enhanced dust shells of Brown & Millar (2003) (bottom). The distance to IRC+10216 has been assumed to be 130 pc. Details of the chemical model used to calculate these profiles are given in Section 2.

(A color version of this figure is available in the online journal.)

enhanced shells of gas in addition to the dust shells of Brown & Millar (2003). Thus, the new model assumes kinematical coupling between the gas and dust in the CSE. The aim is to model the chemistry of the narrow shell-like structures observed in the IRC+10216 outflow by Dinh-V-Trung & Lim (2008) and Guélin et al. (1999) to test the idea that coupling between the gas and dust plays an important role in determining the morphology of the molecular distributions.

The molecular anions C_4H^-, C_6H^-, C_8H^-, and C_3N^- have been recently detected in the envelope of IRC+10216 (for a review of the astrophysical anion detections reported so far, see Herbst & Osamura 2008 and the newly published detections of Gupta et al. 2009). Following these discoveries, we also expand upon the anion chemistry in IRC+10216 studied by Millar et al. (2000, 2007). In particular, the C_nN^- chemistry is reconsidered using the reaction rates between N atoms and carbon-chain anions published by Eichelberger et al. (2007). The possibility that magnesium isocyanide (MgNC) is produced in the outer CSE by gas-phase chemistry is also examined.

2. THE CHEMICAL MODEL

2.1. Physics

The new chemical model for IRC+10216 is based on the model of Miller et al. (2000). The underlying density distribution

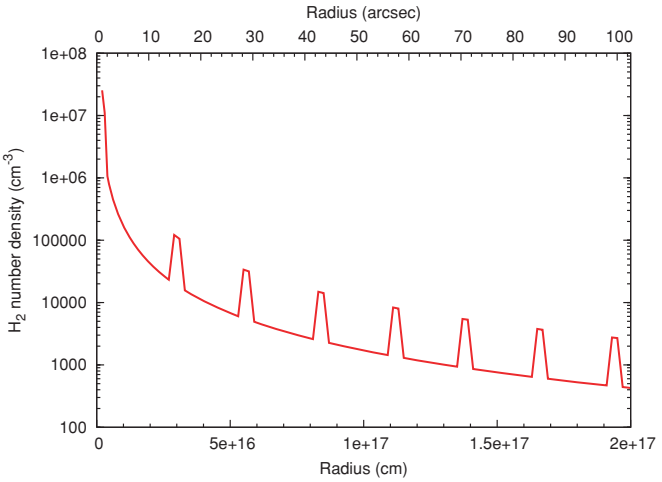

Figure 2. Radial H_2 density profile used in the model.

(A color version of this figure is available in the online journal.)

in the CSE is derived using a mass-loss rate of 1.6×10^{-5} $M_\odot$ yr^{-1} (after Men'shchikov et al. 2001), and assuming that the matter expands in a spherically symmetric outflow with a velocity of 14 km s^{-1}. The resulting gas number density profile $n(r)$ falls as $1/r^2$, added to which is a series of steplike density enhancements of the form $\beta n(r)$. Based on the dust shell parameters deduced from scattered light observations by Mauron & Huggins (2000), each shell is 2″ thick with an intershell spacing of 12″, which corresponds to a timescale of approximately 530 years between successive episodes of enhanced mass loss. The parameter β is set to 5 for all shells in the present model (see Section 2.3). To convert between physical length units and angular distances on the sky, the distance to IRC+10216 is taken to be 130 pc (after Men'shchikov et al. 2001). The chosen shell parameters are not intended to provide an accurate representation of the dust shell structure observed in IRC+10216 (for which a three-dimensional, time-dependent model of the gas and dust in the envelope would be required), but to permit the study of the general effects on the chemical model of the addition of density-enhanced gas and dust shells. The radial H_2 gas density distribution used in the model is shown in Figure 2. The H_2 is assumed to be completely self-shielded in the regions of interest in the CSE so that $n_{H_2}(r) \approx n(r)$.

The adopted temperature profile is based on an empirical fit to the gas kinetic temperature profile derived by Crosas & Menten (1997), and takes the form

$$T(r) = \max\left[\left(\frac{2.81 \times 10^{15}}{r}\right)^{4.7} + \left(\frac{3.34 \times 10^{17}}{r}\right)^{1.05}, 10\right] \quad (1)$$

with a lower limit of 10 K to prevent the temperature becoming unrealistically low in the outer envelope. Parent species (with abundances shown in Table 1) are injected into the model at the inner radius of $r_i = 10^{15}$ cm, where the gas density is 8.6×10^7 cm^{-3}. At this radius, the gas kinetic temperature is 575 K and the interstellar radiation field is attenuated by an effective radial extinction of 47 magnitudes in the V band. Initial abundances are the same as in Millar et al. (2000), with the addition of Mg (see Section 3.3), and with C_2H_2 and HCN abundances taken from the recent measurements by Fonfria et al. (2008).

The standard interstellar radiation field (Draine 1978) is assumed to impinge on the outside of the CSE from all directions. The extinction is calculated for the underlying $1/r^2$ density distribution of the CSE using the approach of Jura &

Table 1
Initial Fractional Abundances of Parent Species Relative to H_2

Species	Initial Abundance
He	1.5×10^{-1}
C_2H_2	8.0×10^{-5}
CH_4	2.0×10^{-6}
H_2S	1.0×10^{-6}
HCN	2.0×10^{-5}
NH_3	2.0×10^{-6}
CO	6.0×10^{-4}
CS	4.0×10^{-6}
N_2	2.0×10^{-4}
Mg	1.0×10^{-5}

Morris (1981). Additional terms are added to the extinction due to the contributions of the density-enhanced shells (for further details of the extinction calculation in the presence of dust shells, see Brown & Millar 2003).

2.2. Chemistry

The chemical reaction network is based on that used by Petrie et al. (2003) and Millar et al. (2007). The reaction rates have been updated to be consistent with those in the (dipole-enhanced) RATE06 database (Woodall et al. 2007). Additional new reactions from RATE06 for those species in the Petrie et al. (2003) model have also been added. The following reactions were deleted from the reaction network in order to increase computational speed, with negligible effect on the chemistry of the species of interest in this study: those with activation energies greater than 300 K; those reactions involving H_3O^+ as a reagent (except for $H_3O^+ + e^-$); those with H_2^+ as a reagent (except for $H_2^+ + e^-$ and $H_2^+ + H_2$); and any reactions involving C^-, S^-, CO^+, HOC^+, $C_2H_6^+$, and C_2H_5.

Carbon-chain species, hydrocarbons, cyanopolyynes and their associated anions and cations are of principal importance for the chemistry of this study. The following species are among those included in the chemical model: carbon chains C_n ($n = 1-23$), C_n^+ ($n = 1-23$), C_n^- ($n = 3-23$); $C_{2n-1}^{(+)}S$ ($n = 1-3$); $HC_{2n-1}S$ ($n = 1-3$); hydrocarbons $C_nH^{(+/-)}$ ($n = 2-23$), $C_nH_2^{(+)}$ ($n = 1-23$), C_nH_3 ($n = 1-4$), $C_nH_3^+$ ($n = 1-23$), C_nH_4 ($n = 1-3$), $C_nH_4^+$ ($n = 1-9$), $C_nH_5^+$ ($n = 2-9$) and cyanopolyynes $C_{2n-1}N^{(+/-)}$ ($n = 1-11$), $HC_{2n-1}N$ ($n = 1-12$), $HC_{2n-1}N^+$ ($n = 1-11$) $H_2C_{2n-1}N^+$, ($n = 1-11$), $H_3C_{2n-1}N^+$ ($n = 2-5$).

Due to the current interest in molecular anions in IRC+10216 (e.g., Millar et al. 2007; Remijan et al. 2007; Cordiner et al. 2008; Thaddeus et al. 2008), the anion chemistry has been extended to include C_nH^- down to $n = 2$, utilizing the radiative electron attachment rates from Herbst & Osamura (2008). The following additional CN^- and C_2H^- formation reactions have been included:

$$HCN + H^- \longrightarrow CN^- + H_2 \quad (2)$$

$$C_2H_2 + H^- \longrightarrow C_2H^- + H_2. \quad (3)$$

The rate coefficient used for Equation 2 (3.8×10^{-9} cm^3 s^{-1}) is an estimate taken from Prasad & Huntress (1980). For Equation 3, the rate coefficient (4.42×10^{-9} cm^3 s^{-1}) was measured experimentally by Mackay et al. (1977). These proton-transfer reactions are likely to be important in the model due to the large HCN and C_2H_2 abundances in the stellar outflow.

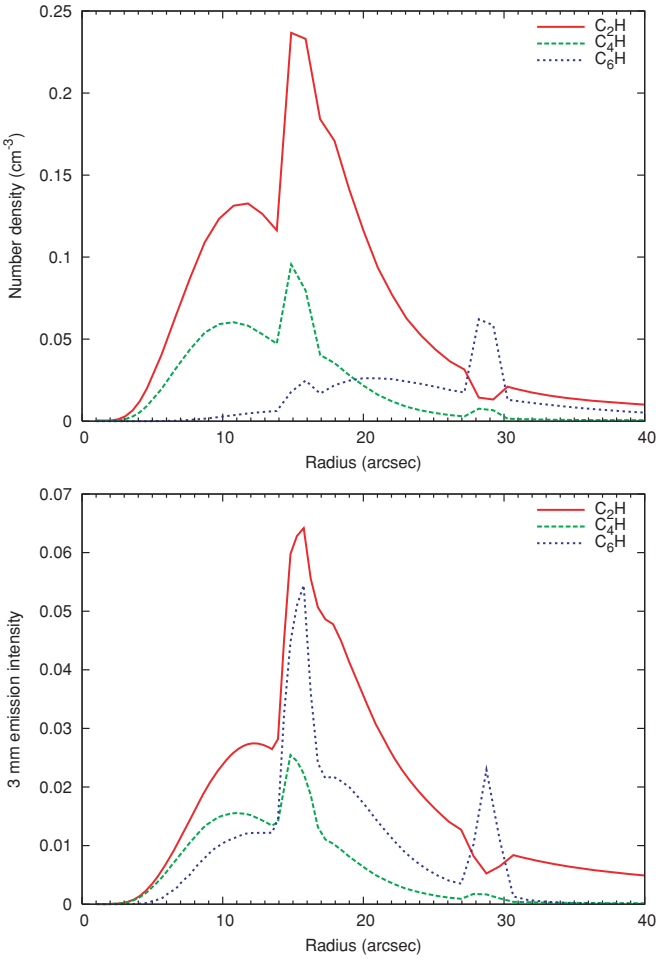

Figure 3. C_2H, C_4H, and C_6H modeled radial abundance profiles (top) and 3 mm emission intensity profiles (multiplied by constant scaling factors for display; bottom).

(A color version of this figure is available in the online journal.)

H^- is produced in the model mainly by the cosmic-ray (CR) dissociation of H_2 ($H_2 + CR \longrightarrow H^+ + H^-$). This reaction is slow (with a rate coefficient of 3.9×10^{-21} cm^3 s^{-1}; Prasad & Huntress 1980), but provides the main source of H^- in the inner envelope. Interior to the second density-enhanced shell ($r \lesssim 2 \times 10^{16}$ cm), the modeled H^- abundance is about 10^{-8} cm^{-3}. Other reactions similar to Figure 3 were studied by Mackay et al. (1977), who found that many different molecular anions could receive a proton from C_2H_2 at rapid rates ($\sim 10^{-9}$ cm^3 s^{-1}), resulting in the production of C_2H^-. However, it is presently unknown whether reactions occur between C_2H_2 and the carbon chain anions C_n^- and C_nH^-. In light of an observational upper limit for $N(C_2H^-)$ in IRC+10216, Cordiner et al. (2008) deduced that these reactions probably do not proceed rapidly.

Dominant anion destruction mechanisms are by reaction with H and C^+ and by photodetachment. Photodetachment rates were calculated according to Equation (2) of Millar et al. (2007). As a result of its large electron detachment energy, the CN^- photodetachment rate thus calculated is $\sim$100 times less than the value in the RATE06 database.

Carbon chain anions C_n^- ($n = 2-7$), and C_nH^- ($n = 2, 4, 6$) have been shown to react with atomic nitrogen and result in the formation of products that include the nitrile anions C_nN^- ($n = 1, 3, 5$) (Eichelberger et al. 2007). We have included these reactions in the model as part of our

investigation into the possible mechanisms for the formation of CN^- and the recently discovered C_3N^- (Thaddeus et al. 2008). Branching ratios were calculated from Eichelberger et al.'s (2007) original experimental data by V. M. Bierbaum (2008, private communication). The branching ratio for the associative electron detachment (AED) product channel could not be derived from the experimental data, so we have assumed, arbitrarily, a ratio of 0.5. This assumption constitutes potentially the most significant source of error in these reaction rates.

Mutual neutralization reactions between anions and cations were shown by Lepp & Dalgarno (1988) to have important effects on interstellar chemistry. Thus, reactions of the kind

$$X^+ + Y^- \longrightarrow X + Y \quad (4)$$

have been included for the 20 most abundant cations (X^+), and for all anions (Y^-), in the model, with a rate coefficient of $7.5 \times 10^{-8}(T/300)^{-0.5}$ cm^3 s^{-1} (see Harada & Herbst 2008, for example).

The final chemical network contains 426 gas-phase species coupled by 5539 reactions.

2.3. Evolution of the Shells

Initially, the rate equations are solved as a function of radius (in the same way as Millar et al. 2000), starting from $r_i = 10^{15}$ cm and moving out to $r_f = 3 \times 10^{18}$ cm where photodissociation destroys all the molecules (apart from H_2). Then, in a separate routine the chemical abundances inside the density-enhanced shells are calculated as a function of radius. The chemical rate equations of a density-enhanced packet lying halfway between a shell's inner and outer radius (at a radius r_p with density $(\beta + 1)n(r_p)$) are solved, starting from r_i and moving out to 2×10^{17} cm where the density is sufficiently low that the shell no longer makes any significant contribution to the total amount of matter in the model. The motion of the density-enhanced shells in the outflow are followed so that they move outward over time, synchronized with the outward radial motion of the dense packet. The radiation field is recalculated for the dense packet at each time step, taking into account the new positions of all the shells. The density factor (β), the intershell spacing and the shell thickness are identical for every shell so that the chemical abundances calculated for the dense packet at a given radius represent the abundances in a density-enhanced shell centered at that radius.

2.4. Model Variations

The effects on the model results of variations in the mass-loss rate, radiation field strength, gas-to-dust ratio, shell thickness, intershell spacing, density-enhancement factor and stellar distance have been analyzed. The results presented in this study are for the model that uses the parameters that we believe best match the observational constraints. Modification of these parameters, particularly those that affect the radiation field strength, can significantly alter the radial abundance profiles calculated by the model. However, under such circumstances the main conclusions of this study remain the same. The location of the 15″ density-enhanced shell has been fixed in order to best reproduce the observational data, which may be considered a contrivance of the model. However, in Figure 8 of Mauron & Huggins (2000), this can be identified as the radius at which the first distinct dust shells occur.

To permit comparison between this model and previous models published in the literature (which do not include density-enhanced gas and dust shells), we have also run the model without any density-enhanced shells (i.e., $\beta = 0$) and also with the density-enhanced dust shells of Brown & Millar (2003) to produce the data shown in Figure 1.

2.5. Molecular Excitation

To facilitate comparison of the model results with observed maps of molecular microwave emission line flux, the rotational excitation of some of the molecules of interest has been calculated as a function of radius using a modified version of the mmline computer code (described by Justtanont et al. 1994). The central stellar radius was taken to be 3.1×10^{13} cm and the temperature 2650 K (derived from Men'shchikov et al. 2001). The dust opacity was taken from Figure 6 of Men'shchikov et al. (2001). Due to the lack of published collisional excitation rates and vibrational transition strengths, only a rough estimate of the rotational excitation is possible for most molecules. For C_2H and C_2H^-, the HCO^+ rates from Flower (1999) are used, and for C_4H, C_4H^-, C_6H, and C_6H^- the HC_3N rates from Green & Chapman (1978) are used. For C_6H and C_6H^-, the rates have been extrapolated up to $J = 31$. The collisional rates used are for closed electronic-shell species so the spectroscopic structure of the corresponding (closed electronic-shell) anions has been used for the calculations of the excitation of the open-shell C_2H, C_4H, and C_6H radicals. This approximation is reasonable because the structure of these hydrocarbon anions and neutrals are very similar. Only the $^2\Pi_{1/2}$ states have been considered for the neutral hydrocarbons; the population of the $^2\Pi_{3/2}$ states is not expected to significantly affect the relative populations of the states of interest here. Rotational Einstein A coefficients were calculated using dipole moments from Woon (1995) and Blanksby et al. (2001) for the neutrals and the anions, respectively. Infrared (IR) pumping of rotational levels has been calculated through consideration of the radiative excitation of a single vibrational state $\sim$10 μm above the ground state (e.g., Bieging et al. 1984). C_2H has been calculated to have a strong vibrational transition ($A = 0.6$ s^{-1}) at 12.5 μm (Tarroni & Carter 2004), which we assume to also occur in C_2H^-. The vibrational spectra of C_4H, C_6H and their associated anions are less well known. For these species, a transition has been assumed to occur at 12.5 μm with $A = 1$ s^{-1}. IR pumping has a significant effect on the molecular excitation, but changes in the vibrational transition wavelengths and Einstein A coefficients by up to an order of magnitude do not significantly affect the results of the present study. To assess the impact of errors in the collisional excitation rates on the calculated molecular emission profiles, the rates were varied by an order of magnitude either way. The overall features of the emission profiles remained the same.

3. RESULTS

3.1. Molecular Radial Abundance and Intensity Distributions

The upper panel of Figure 3 shows the calculated radial abundance profiles for the hydrocarbons C_nH ($n = 2, 4, 6$). Comparison with Figure 1 shows the impact of the density-enhanced shells on these species. A prominent effect of the shells is to raise of the abundances relative to the surrounding CSE due to the increased gas density. The photon-induced hydrocarbon chemistry is suppressed very near to the star by the dust shell at a radius of $r = 1''$ which provides additional shielding of C_2H_2 from photodissociation. The abundances all reach a peak in the shell at $r = 15''$. However, this is not where C_6H reaches its

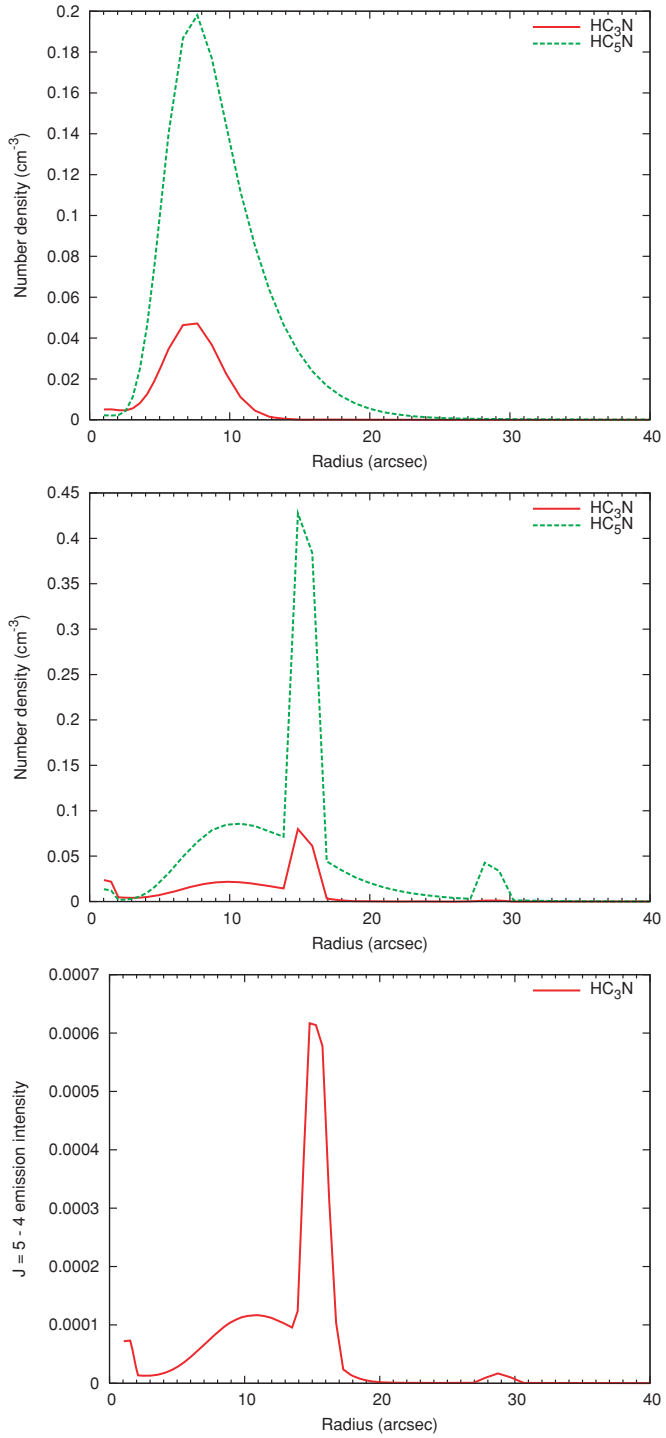

Figure 4. Modeled radial abundance profiles for HC_3N and HC_5N in the absence of density-enhanced shells (top) and with density-enhanced shells (middle). The bottom panel shows the modeled HC_3N $J = 5$–4 intensity profile calculated in the presence of density-enhanced shells.

(A color version of this figure is available in the online journal.)

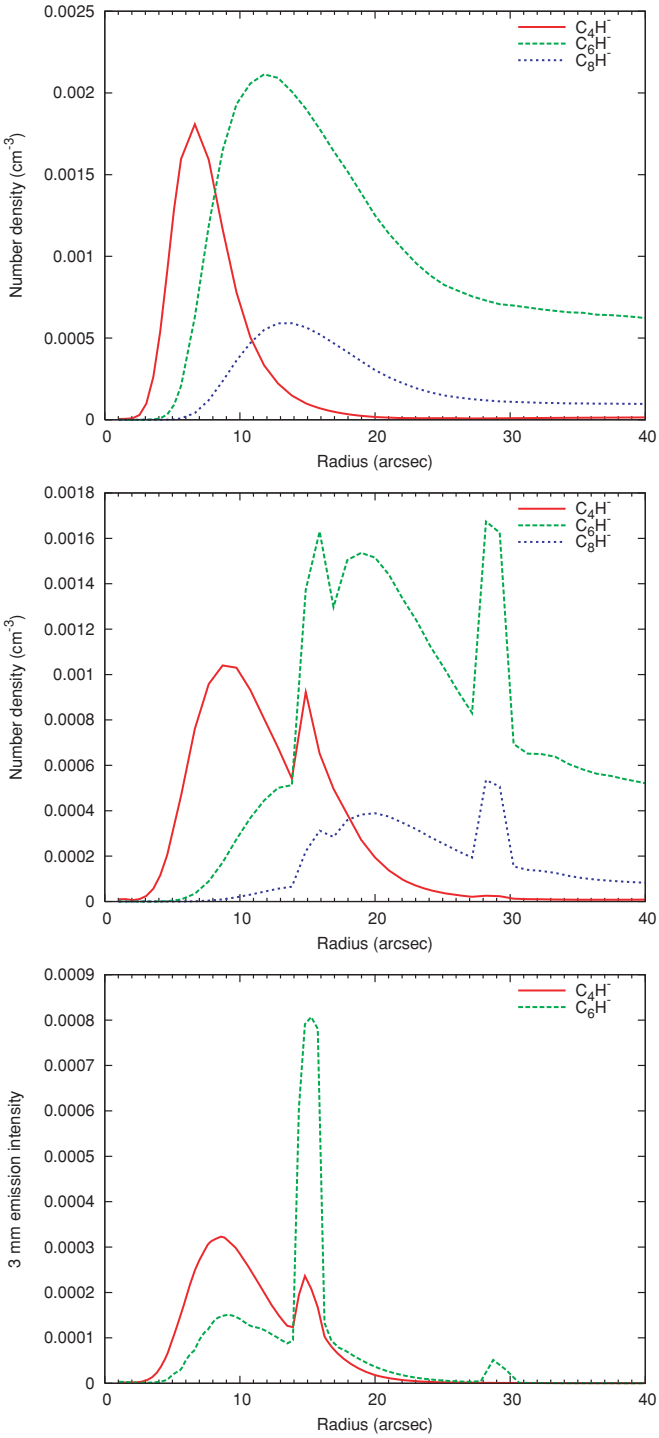

Figure 5. Modeled radial abundance profiles for the hydrocarbon anions C_4H^-, C_6H^-, and C_8H^- in the absence of density-enhanced shells (top) and with density-enhanced shells (middle). C_4H^- and C_6H^- 3 mm emission intensity profiles are shown in the bottom panel.

(A color version of this figure is available in the online journal.)

greatest abundance, which occurs in the third density-enhanced shell at $r = 29''$. As shown in the middle panel of Figure 4, HC_3N and HC_5N both reach their greatest abundances in the $15''$ shell. CR-induced chemistry also results in the synthesis of a significant amount of HC_3N in the innermost ($r = 1''$) shell (through the reaction HCN + CRPHOT $\longrightarrow$ CN + H, followed by CN + C_2H_2 $\longrightarrow$ HC_3N + H). The anions C_4H^-, C_6H^-, and C_8H^- (shown in Figure 5) do not reach their maximum abundances in the $15''$ shell; C_4H^- peaks at a similar radius to the model with no shells whereas C_6H^- and C_8H^- peak in the $29''$ shell.

Molecular abundances tend to peak within the density-enhanced shells because the increased density raises the abundances of chemical reagents which drives the chemistry at a faster rate. It is not always the case, however, that this raises the abundances of daughter species, as can be seen in Figure 3

where the C_2H abundance is reduced in the $r = 29''$ shell due to the increased densities of atoms and ions (including C, C^+, and N), that it reacts with.

A comparison of the abundance profiles in the models with and without density-enhanced shells shows that, in general, the increased shielding of the CSE from interstellar UV by the dust shells (which inhibits the photochemistry) causes photodissociation of parent species to be less efficient in the inner regions and causes the daughter abundances to rise more slowly with radius, moving the profile maxima outward.

The calculated emission intensities for C_2H, C_4H, C_6H, C_6H^-, and HC_3N (shown in the lower panels of Figures 3–5, respectively) are greatest within the $r = 15''$ density-enhanced shell. C_4H^- reaches maximum intensity near $r = 8''$. The differences between the abundance profiles and the emission profiles for C_6H and C_6H^- are particularly notable. Because the 3 mm emission from these species originates from a high rotational level (around $J = 30$), the strength of the emission is highly dependent on the rate of collisional excitation, and therefore the density. Thus, inside the density-enhanced shells the lower J levels tend to become depopulated in favor of the higher levels.

For C_2H, C_4H, C_6H, and their corresponding anions, two-dimensional emission maps have been constructed from the radial emission profiles by integration along (pencil-beam) lines of sight through the CSE. This calculation assumes spherical symmetry of the CSE and therefore cannot show any of the azimuthal structure in observed emission maps. Nevertheless, these maps (shown in Figure 6) provide a useful means for comparing the main features in the modeled and observed molecular emission.

C_2H and C_6H show a strong, narrow emission ring centered at $15''$, in excellent agreement with observed maps of Guélin et al. (1999). In addition to the observed $15''$ ring, the modeled C_4H emission map shows a thick, strong ring at around $r = 8'$. The patterns for C_4H^- and C_6H^- are similar to their parent neutrals whereas C_2H^- is markedly different: it has a centrally peaked emission map because it is produced predominantly by the reaction of H^- with C_2H_2—the abundances of which are greatest in the (well shielded) inner CSE—rather than by electron attachment to its parent neutral.

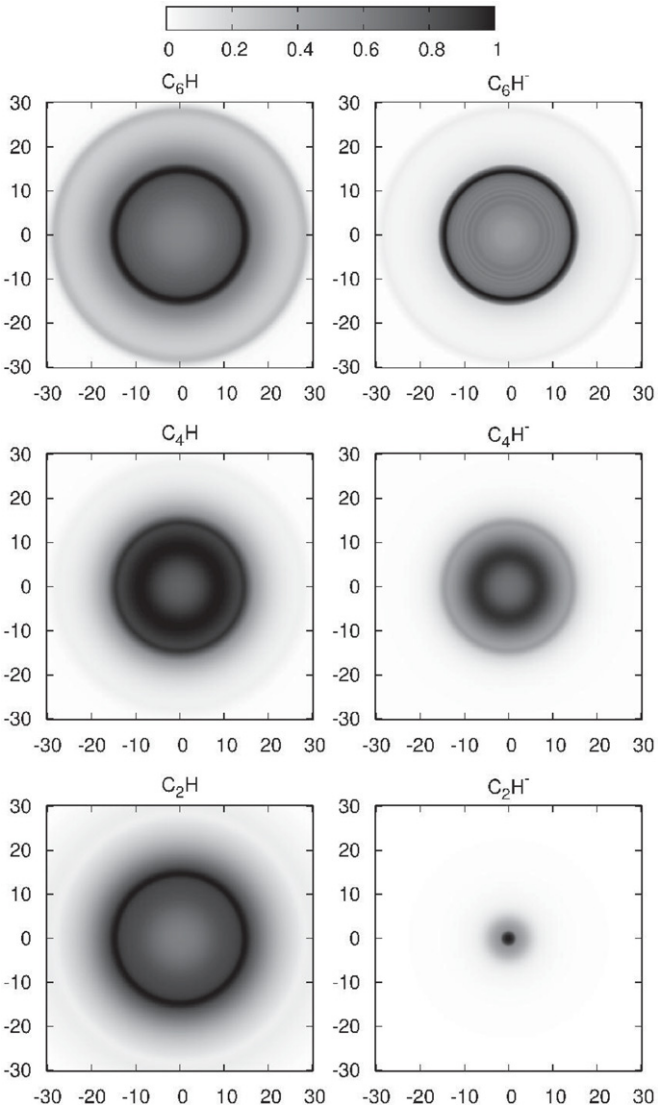

Figure 6. Emission maps for hydrocarbons and their anions, calculated from the modeled radial intensity profiles assuming spherical symmetry of the CSE. The grayscale is set to one at the respective emission maxima of each plot. Spatial units are arcseconds from the central star.

3.2. New Anion Results

Column densities for all anions included in the chemical model are given in Table 2.

Cordiner et al. (2008) identified that the reaction of H^- with HCN (Figure 2) could dominate the synthesis of CN^- in IRC+10216. However, the present study shows that reactions between atomic nitrogen and the carbon chain anions may provide a greater source of CN^-. Upon inclusion of the reactions N + C_n^- and N + C_mH^- into the chemical network (see Section 2.2), the CN^- column density is raised from 1.3×10^{10} to 1.3×10^{12} cm^{-2}. Due to the fact that C_7^- is the most abundant anion involved in these reactions, the dominant formation reaction for CN^- is N + $C_7^- \longrightarrow CN^-$ + C_6. These results are dependent on the values of the branching ratios assumed for the AED reactions. Even if the AED branching ratio is as large as 0.9 (instead of the assumed value of 0.5), the CN^- column density is calculated to be 2.7×10^{11} cm^{-2} and N + C_7^- is still the dominant reaction for CN^- production.

C_3N^- was detected for the first time in IRC+10216 by Thaddeus et al. (2008), who report a column density of 1.6×10^{12} cm^{-2}. If C_3N^- is assumed to be formed only by radiative electron attachment to C_3N, the modeled column density is 1.1×10^{10} cm^{-2}, with a corresponding anion-to-neutral ratio of 0.02%. This would imply that the electron attachment rate used (calculated by Petrie & Herbst 1997) is too small. However, upon inclusion of reactions between nitrogen atoms and anions, the modeled C_3N^- column density rises to 9.0×10^{11} cm^{-2} (which corresponds to an anion-to-neutral ratio of 1.3%), in reasonable agreement with the observed value. The dominant reactions involved in the production of C_3N^- in our present model are N + C_n^- ($n = 5, 6, 7$). If these reactions do indeed dominate the C_3N^- synthesis then the rate of radiative electron attachment to C_3N calculated by Petrie & Herbst (1997) may still be accurate.

Cyanopolyynes C_nN (for $n > 4$), by analogy with the structurally similar linear hydrocarbons C_nH ($n > 5$) studied by Herbst & Osamura (2008), have been assumed to undergo rapid radiative stabilization upon attachment of a free electron so that the rate of radiative electron attachment used in the model is $1.25 \times 10^{-7}(T/300)^{-0.5}$ cm^{-3} s^{-1}. Consequently, C_5N^- and C_7N^- have large modeled column densities of 1.7×10^{13} and

Table 2
Calculated Column Densities of Negatively Charged Species

Species	N (cm^{-2})	Species	N (cm^{-2})	Species	N (cm^{-2})
C_3^-	3.9e10	C_2H^-	5.5e10	CN^-	1.3e12
C_4^-	7.5e12	C_3H^-	1.4e9	C_3N^-	9.0e11
C_5^-	3.2e13	C_4H^-	2.5e13	C_5N^-	1.7e13
C_6^-	5.3e13	C_5H^-	1.2e13	C_7N^-	7.2e12
C_7^-	1.6e14	C_6H^-	9.6e13	C_9N^-	3.6e11
C_8^-	9.6e13	C_7H^-	5.2e13	$C_{11}N^-$	3.7e10
C_9^-	1.1e14	C_8H^-	2.0e13	$C_{13}N^-$	2.6e10
C_{10}^-	4.0e13	C_9H^-	1.6e13	$C_{15}N^-$	1.9e10
C_{11}^-	3.1e13	$C_{10}H^-$	5.2e12	$C_{17}N^-$	1.3e10
C_{12}^-	8.3e12	$C_{11}H^-$	1.4e13	$C_{19}N^-$	8.5e9
C_{13}^-	1.5e13	$C_{12}H^-$	3.1e12	$C_{21}N^-$	5.3e9
C_{14}^-	3.9e12	$C_{13}H^-$	8.4e12		
C_{15}^-	4.6e12	$C_{14}H^-$	1.4e12	CH_2CN^-	2.5e6
C_{16}^-	1.8e12	$C_{15}H^-$	6.4e12		
C_{17}^-	2.5e12	$C_{16}H^-$	1.1e12	H^-	3.3e8
C_{18}^-	1.1e12	$C_{17}H^-$	4.6e12		
C_{19}^-	1.5e12	$C_{18}H^-$	9.4e11	e^-	4.8e15
C_{20}^-	6.9e11	$C_{19}H^-$	3.2e12		
C_{21}^-	1.0e12	$C_{20}H^-$	7.8e11		
C_{22}^-	4.2e11	$C_{21}H^-$	2.1e12		
C_{23}^-	8.1e11	$C_{22}H^-$	5.5e11		
		$C_{23}H^-$	9.9e12		

7.2×10^{12} cm^{-2}, respectively, which correspond to about 8% of the abundance of their neutral parents C_5N and C_7N. Radiative electron attachment dominates the production of these anions in the model, but it seems plausible that reactions between atomic nitrogen and carbon-chain anions longer than those studied by Eichelberger et al. (2007) would also result in fragmentation of the carbon chain. Such fragmentation was observed in the experiments by Eichelberger et al. (2007; who studied carbon chain lengths up to only $n = 7$ carbon atoms), which gave rise to products with carbon chains with lengths from 1 to n. If the fragmentation of carbon-chain anions with $n > 7$ was included in our chemical model, there would be a significant increase in the production rates of the nitrile anions $C_{2n-1}N^-$ ($n = 1-4$), so that these reactions could potentially dominate the production of C_5N^- and C_7N^- as well.

Dense shells in the inner envelope have a significant impact on the C_2H^- radial abundance profile, as shown in Figure 7. C_2H^- is concentrated in the region of the envelope around the $r = 1''$ shell. The presence of this shell raises the C_2H^- column density from 2.3×10^{10} to 5.5×10^{10} cm^{-2}. This anion is unusual in the model because its rate of formation by radiative electron attachment is very slow; it is produced predominantly in the inner envelope as a result of Equation 3 ($H^- + C_2H_2 \longrightarrow C_2H^- + H_2$). This may have important observational consequences because the kinetic temperature of the gas is higher at such radii, which would cause the molecule to exist in a higher state of rotational excitation. Direct comparison of (unresolved) single-dish microwave observations of C_2H^- and C_2H may be made more difficult by the difference in the distributions and therefore the telescope beam-filling factors of these two species. Detailed microwave observations of the spatial distributions of C_2H^- are clearly required in order to confirm this result and determine whether Equation 3 is indeed the dominant production mechanism for this species.

In the new model for the CSE of IRC+10216, the respective anion-to-neutral column density ratios for C_4H, C_6H, and C_8H are calculated to be 1.4%, 7.4%, and 4.5%. The corresponding observational ratios are 0.024%, 6.3% (Cernicharo et al. 2007), and 26% (Remijan et al. 2007). As highlighted above for C_2H, obtaining accurate observational ratios is hindered by the possibility that the anions and neutrals have different spatial distributions within the CSE. Nevertheless, it is clear that our model still severely overestimates the amount of C_4H^- compared with C_4H (see also Herbst & Osamura 2008). It may be the case that the C_4H radiative electron attachment rate calculated by Herbst is too large. Alternatively, C_4H^- may be destroyed more rapidly than our model currently predicts, for example, by reaction with HCN or C_2H_2 (e.g., Equations (2) and (3)). In that case, such reactions would have to be much more rapid for C_4H^- than for C_6H^- and C_8H^-, which could conceivably result from the different electron binding energies of these species (E. Herbst 2008, private communication). Further laboratory and/or theoretical studies are required in order to determine whether the organic anions considered here react with HCN, C_2H_2 or other possible proton-donating molecules.

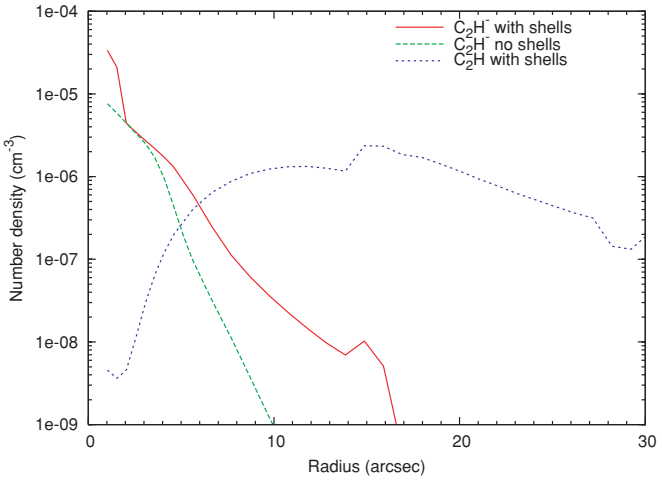

Figure 7. Modeled C_2H^- number density profiles with and without density-enhanced shells. The C_2H abundance is also shown, multiplied by 10^{-5} for display.

(A color version of this figure is available in the online journal.)

Anion-to-neutral ratios of the C_n and C_nH species are typically slightly greater in the present model compared to the no-shells (NS) model. This is largely attributable to the increased electron abundances inside the dominant $15''$ shell which leads to increased rates of electron attachment. Figure 8 shows the electron abundances as a function of radius. The density-enhanced shells cause increased shielding of the gas from photoionization which results in electron abundances which are a factor ~2 lower between $r = 20''$ and $100''$. Inside the shells at these radii, contrary to the $15''$ shell, the electron densities are up to an order of magnitude lower than the surrounding CSE. Beyond ~$100''$ where the density becomes very low, the shells begin to have a negligible effect on the photoionization rate as shown for atomic carbon in Figure 8. Accordingly, the electron abundances of the models with and without shells converge at this radius.

3.3. MgNC

A number of metal-containing molecules have been detected in IRC+10216. While some of these, for example NaCl, KCl, and AlCl, are expected to be abundant in the local thermodynamic equilibrium region and have spatial distributions that

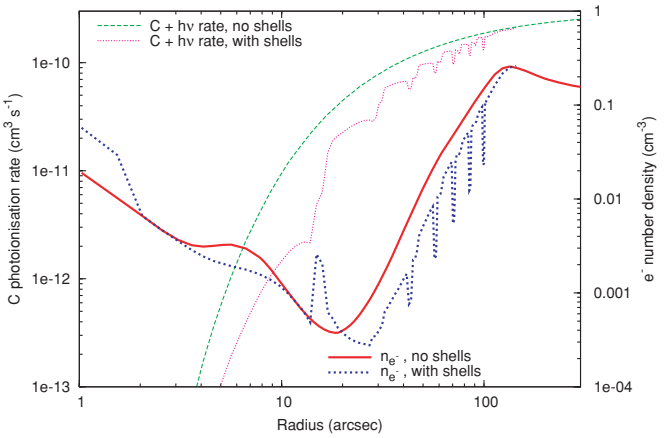

Figure 8. Electron number density profiles for models with and without density-enhanced shells. The atomic carbon photoionization rates (C + $h\nu$) for the two models are also plotted.

(A color version of this figure is available in the online journal.)

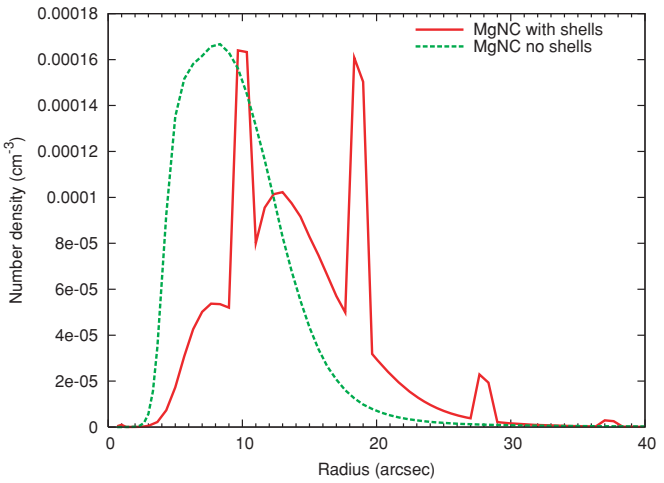

Figure 9. Modeled MgNC number density profiles with and without density-enhanced shells.

(A color version of this figure is available in the online journal.)

peak on the star, other species, particularly the cyanides and isocyanides such as MgCN, MgNC, and AlNC, have shell-like distributions on scales very similar to the cyanopolyynes (Ziurys et al. 2002). Two possibilities exist to account for the presence of these species in the outer envelope: either they form in the gas phase from metals that have not been incorporated into dust in the inner envelope or they have been released from grains by erosion processes in the outer envelope.

In order to test the hypothesis that metal isocyanides are formed by gas-phase chemistry, we have investigated the synthesis of MgNC via radiative association reactions between Mg^+ and the cyanopolyynes (Dunbar & Petrie 2002):

$$Mg^+ + HC_nN \longrightarrow HC_nNMg^+ + h\nu \qquad (5)$$

(with $n = 3, 5, 7, 9$), followed by dissociative recombination reactions of the form

$$HC_nNMg^+ + e^- \longrightarrow MgNC + C_{n-1}H. \qquad (6)$$

Figure 9 shows the radial abundance (cm^{-3}) of MgNC in both the presence and absence of shells. In these calculations, we adopt an initial Mg/H_2 abundance ratio of 10^{-5}—the derived abundances and column densities are directly proportional to this ratio. The effect of the density-enhanced shells is, once again, to move the peak of the distribution outward and to concentrate the abundance to the peaks of the gas density, in this case with almost equal peaks in the 15″ and 29″ shells. The total MgNC column density is calculated to be 5.7×10^{13} cm^{-2}, compared to observed values of $(0.93–5)\times10^{13}$ cm^{-2} (Guélin et al. 1995; Highberger & Ziurys 2003). The dominant formation reaction is with HC_7N which, despite its smaller abundance, has the largest radiative association rate coefficient (Figure 5), $6.59\times10^{-9}(T/300)^{-0.47}$ cm^3 s^{-1} (Dunbar & Petrie 2002).

It was suggested by Dunbar & Petrie (2002) that the inclusion of Equation 5 into chemical models for IRC+10216 might significantly reduce the abundances of the species HC_nN and help to reconcile the discrepancy between modeled and observed HC_nN column densities. In the present model, we find that the reaction of Mg^+ with HC_5N, HC_7N, and HC_9N results in only ∼1% reduction in their calculated column densities, which does not significantly improve the match with observations. However, the depletion of these species is dependent (in a roughly linear fashion) on the initial Mg abundance employed.

4. DISCUSSION

Compared to previous chemical models of IRC+10216 (e.g., Nejad & Millar 1987; Cherchneff et al. 1993; Millar et al. 2000; Brown & Millar 2003; Agúndez et al. 2008), the model presented here is unique in the inclusion of density-enhanced shells of gas and dust. The shells included in our model have physical parameters similar to the dust shells observed by Mauron & Huggins (2000). As expected, the modeled column densities differ from those calculated in the model by Millar et al. (2000, referred to hereafter as MHB). Table 3 gives the column densities for these two models for 33 species for which observational column densities have been published. To highlight the effect of the density-enhanced shells on the chemistry and to permit comparison with models without density-enhanced shells, the column densities from the present model with no density-enhanced shells (referred to as NS), are also given. The column densities calculated by the three different models are generally in good agreement with observations, especially given the complex morphology of the source.

Notable differences between the MHB and NS models include a substantial reduction in the HC_3N/HC_5N column density ratio in the new model due to the enhanced photodissociation rate used for HC_3N (from the RATE06 database). The C_3N abundance is reduced as well because it is produced predominantly from HC_3N (via an alternative photodissociation channel). The carbon chains C_6H, C_7H, and C_8H, the cyanopolyynes HC_5N, HC_7N, and HC_9N and also CN are significantly more abundant in the present models than MHB. This is primarily due to the increased initial abundances of the parent species C_2H_2 and HCN (Fonfria et al. 2008) to which their chemistry is closely coupled (see Millar & Herbst 1994). C_7H and C_8H are also more abundant as a result of the addition of C_6H^- to the chemical network which undergoes associative detachment with H to form C_6H_2. C_6H_2 reacts with C to produce C_7H or with C_2H to produce C_8H_2, which is photodissociated to C_8H.

Among the 33 chemical species listed in Table 3, 12 show calculated column densities that differ from observations by more than a factor of 10. In the present model, the moderate-to-large-sized hydrocarbons and cyanopolyynes C_4H_2, C_5N, C_6H, C_8H, and HC_9N might be considered to have column

Table 3
Comparison Between Column Densities from the Present Model, the Present Model Including no Density-Enhanced Shells (NS), the Model by Millar et al. (2000, MHB), and Observations

Species	Present	NS	MHB	Observation	Reference
C	2.5e16	2.7e16	1.0e16	1.1e16	1
C_2	2.6e15	2.6e15	9.9e15	7.9e14	2
C_2H	5.6e15	6.3e15	5.7e15	3-5e15	1
CN	2.2e15	2.6e15	1.0e15	1.1e15	2
HCO^+	3.1e12	3.0e12	2.4e12	3e12	1
C_3	3.4e14	2.6e14	6.5e14	1e15	1
C_3H	1.6e14	1.2e14	1.4e14	3-7e13	1, 3
C_3H_2	1.0e14	5.6e13	2.1e13	2e13	1
CH_2CN	2.0e13	1.7e13	6.9e12	8.4e12	4
C_3H_4	1.9e12	5.7e11	4.0e12	1.6e13	4
CH_3CN	3.9e12	3.6e12	3.4e12	6-30e12	1, 4
C_4H	1.7e15	1.8e15	1.0e15	2-9e15	1
C_4H^-	2.5e13	2.1e13	···	7.1e11	5
MgNC	5.7e13	6.6e13	···	0.93-5e13	6, 7
C_4H_2	8.0e15	6.1e15	2.9e15	3-20e12	1
C_3N	7.0e13	5.7e13	3.2e14	2-4e14	1
C_3N^-	9.0e11	7.7e11	4.0e11	1.6e12	8
HC_3N	6.7e14	4.8e14	1.8e15	1-2e15	1
CH_2CHCN	2.6e11	6.6e10	1.1e11	5.1e12	4
C_2S	4.1e13	4.4e13	3.5e13	9-15e13	9, 10
C_5	5.1e14	6.3e14	7.5e14	1e14	1
C_5H	1.9e14	2.0e14	8.7e13	2-50e13	1
C_3S	1.5e14	1.7e14	6.7e12	6-11e13	9, 10
C_6H	1.3e15	1.5e15	5.8e14	6.6e13	5
C_6H^-	9.6e13	1.1e14	···	4.1e12	5
C_5N	2.4e14	2.5e14	1.4e14	3-6e12	1, 3
HC_5N	3.5e15	2.7e15	7.1e14	2-3e14	1
C_7H	3.7e14	3.2e14	4.5e13	1-2e12	1, 3
C_5S	1.8e14	1.7e14	···	2.5e13	10
C_8H	4.1e14	4.9e14	1.1e14	5e12	1
C_8H^-	2.0e13	2.1e13	2.7e13	2e12	11
HC_7N	1.4e15	1.3e15	2.2e14	1e14	1
HC_9N	8.5e14	8.0e14	5.8e13	3e13	1

Notes. References. (1) See references in Table 5 of Millar et al. (2000); (2) Bakker et al. (1997); (3) Cernicharo et al. (2000); (4) Agúndez et al. (2008); (5) Cernicharo et al. (2007); (6) Guélin et al. (1995); (7) Highberger & Ziurys (2003); (8) Thaddeus et al. (2008); (9) Cernicharo et al. (1987); (10) Bell et al. (1993); (11) Remijan et al. (2007).

densities that are discrepantly greater than the observations. By reducing the gas-to-dust ratio G to 50 (from the present value of 200), these discrepancies are eliminated due to the retardation of the C_2H_2 and HCN photochemistry as a consequence of increased dust extinction. The only species to be detrimentally affected by such a reduction in G are C_3N and C_3N^-, and as mentioned previously, the chemistry involving these species is not completely understood at present. Taking $G = 50$ may be too low however, because values from the literature (see Table 5 of Men'shchikov et al. 2001) are typically in the range 200–1000. It is plausible that other factors might contribute toward a reduction in the photochemical yields, such as a reduced incident radiation field strength (see Millar & Herbst 1994) and/or lower initial C_2H_2 and HCN abundances, to bring the model results into better agreement with observations. Changes in the rates of the reactions involved in the synthesis of moderate-to-large-sized hydrocarbons and cyanopolyynes could also help to resolve some of the discrepancies between the current model results and observations. For example, the reactions of the kind $C_2H + HC_{2n+1}N \longrightarrow HC_{2n+3}N + H$ and $C_2H + C_nH_2 \longrightarrow C_{n+2}H_2 + H$ are crucial for the synthesis of successively larger species in the model, and the rates of these reactions are only known, at best, to within a factor of 2. Similarly, the photodissociation rates of many of the larger species in the model are calculated only from estimated cross-sections.

It has been brought to our attention by the referee that in a recent study of narrow submillimeter emission lines from IRC+10216 by Patel et al. (2008), a lower limit to the abundance of CS in the inner envelope of 9.3×10^{-6} was derived. This is significantly greater than our adopted abundance of 4.0×10^{-6}. Thus, we have investigated the impact on our model of raising the initial CS abundance to 1.0×10^{-5}. We find that the only species to be appreciably affected are those containing sulfur and those whose chemistries are closely related to the sulfur-containing molecules. The column densities of HCS, OCS, H_2CS, and C_nS (for $n = 1-5$) scale approximately linearly with the initial CS abundance. The C_3 and C_3H column densities are raised by about 50%, mainly as a result of the photodissociation of C_4S to produce C_3 + CS. The OH column density increases by a similar fraction due to the hydrogen-transfer reaction of HCS with O. No other species in Table 3 have column densities that are significantly affected by the increase in the initial CS abundance.

The inclusion of density-enhanced shells in the model has a profound impact on the calculated radial abundance distributions, both through the extinction effect of the shells which modifies the photochemical reaction rates, and through the effects of their increased densities which accelerate the binary chemical reactions. However, the impact of the shells on the total column densities is generally rather small; even though the chemical abundances may vary by over an order of magnitude inside the shells, the fact that the shells are narrow compared to the radial extent of the CSE means that they contribute toward only a modest fraction of the total column densities. Species whose chemistries are closely linked to the radiation field strength are most affected by the shells, for example C_3H_4 and CH_3CHCN (whose dominant destruction channels are by photodissociation), are shielded from dissociating radiation out to a larger radius by the increased extinction. The enhanced shielding in the envelope also reduces the ionization rate, resulting in up to an order of magnitude reduction in the electron and C^+ column densities at certain radii.

A primary motivation of this study is to examine whether the structure observed by Dinh-V-Trung & Lim (2008) in HC_3N and HC_5N maps of IRC+10216 is consistent with their suggestion that the gas and dust are coupled, sharing a similar density distribution. The inclusion of density-enhanced shells in our model results in peaks in the radial number density distributions of molecules within the shells, which shows that density enhancements in the molecular gas are able to produce small-scale structure in the molecular distributions similar to those observed.

When molecular excitation is taken into account, the emission intensity profiles for C_2H, C_4H, C_6H, and HC_3N all peak inside the dense shell at 15″. This finding is consistent with the 3 mm maps of these species made by Guélin et al. (1999) and Lucas & Guélin (1999) and shows that the presence of dense shells can cause the modeled molecular abundances to peak around the same radius and in a narrow region corresponding to the radius and thickness of the density enhancement. The simulated emission maps (Figure 6) show a similar picture for C_2H and C_6H. However, the inner broad intensity maximum of the C_4H

radial profile results in a $\approx 5''$ wide, intense emission ring inside of the density-enhanced $15''$ ring, which is not seen in the Guélin et al. (1999) map. Possible explanations for this discrepancy might be that the excitation of C_4H favors its observation in the narrow shell (contrary to the crude excitation analysis we performed), or that the interferometer used in the observations failed to detect the broader structure of the inner ring.

In the model, the gas and dust share identically shaped density profiles which requires that the gas and dust must be dynamically coupled. This is contrary to the theory (see Truong-Bach et al. 1991; Mauron & Huggins 2000) that radiation pressure accelerates the circumstellar dust to a radial drift velocity $\sim$2 km s^{-1} faster than the gas. Possible coupling mechanisms may include thermal and turbulent motion of the gas and dust. Future models may need to include a detailed analysis of the coupling between the gas and dust shells.

The shells used in the model represent a gross simplification of the dust shell structure observed in IRC+10216 by Mauron & Huggins (2000). However, the results presented here—that the maximum abundances of species containing carbon chains match the peaks in the circumstellar dust distribution—should be generally applicable to more complex representations of the density structure of the CSE. The density-dependent nature of molecular excitation means that detailed excitation calculations are required to determine the relationship between observed emission intensity and molecular abundance distributions. In our model, the temperature distribution of the gas is assumed to be continuous, with the assumption that the density-enhancements are in thermal equilibrium with the surrounding medium. More detailed observations of the gas and dust will be required to determine if this assumption is realistic. In addition, accurate collisional and vibrational excitation rates will be required in order to more accurately calculate the rotational excitation of the molecules considered.

5. CONCLUSION

Density-enhanced shells of gas and dust have a significant impact on the calculated radial distributions of molecules in the expanding envelope of IRC+10216. Based on the suggestion by Dinh-V-Trung & Lim (2008) that the gas and dust are coupled, we included in a new model for the CSE a set of density enhancements with parameters based on the dust shell observations by Mauron & Huggins (2000). Photochemistry is delayed to greater radii due to increased shielding by the dust shells. Density enhancements in the gas result in molecular abundances that peak inside the narrow shells, showing that the clumpy structure observed in HC_3N and HC_5N may be the result of density enhancements in the molecular gas. The calculated emission intensity profiles for C_2H, C_6H, and HC_3N all peak within a narrow band about $15''$ from the central star, which is consistent with detailed emission maps of these species. The emission profile for C_4H has a broad maximum around $8''$ that is not present in observed maps, which may be indicative of a need for further improvements in the model.

The ethynyl anion C_2H^- and the nitrile anions $C_{2n-1}N^-$ (for $n = 1, 2, 3, 4$) have been calculated to reach observable abundances in the CSE. For the smaller nitrile anions for which radiative electron attachment is slow (i.e., CN^- and C_3N^-), this result is uncertain due to the unknown product branching ratios in the AED channels of the reactions N + C_m^- and N + C_mH^-. Further laboratory measurements (including up to at least $m = 10$) will be required in order to confirm the importance of these reactions in anion astrochemistry. C_2H^- is predicted to be produced in abundance in the inner CSE (at much smaller radii than the other anions in the model), as a product of the reaction of H^- with C_2H_2. Other possible proton transfer reactions of this kind (i.e., $XH + Y^- \longrightarrow X^- + YH$, for the anions listed in Table 2) also need to be considered for possible inclusion in future anion chemical networks.

Our chemical models produce MgNC with a peak abundance in the outer envelope. Dependent on the initial Mg abundance used, the observed MgNC column density matches observation, which shows that gas-phase chemistry is a viable route to the formation of this species.

We gratefully acknowledge Veronica Bierbaum and Eric Herbst for their contributions to this work regarding the calculation of branching ratios for reactions between anions and nitrogen atoms. M.A.C. thanks QUB for financial support. Astrophysics at QUB is supported by a grant from the STFC.

REFERENCES

Agúndez, M., Fonfría, J. P., Cernicharo, J., Pardo, J. R., & Guélin, M. 2008, A&A, 479, 493
Bakker, E. J., van Dishoeck, E. F., Waters, L. B. F. M., & Schoenmaker, T. 1997, A&A, 323, 469
Bell, M. B., Avery, L. W., & Feldman, P. A. 1993, ApJ, 417, 37
Bieging, J. H., Chapman, B., & Welch, W. J. 1984, ApJ, 285, 656
Blanksby, S. J., McAnoy, A. M., Dua, S., & Bowie, J. H. 2001, MNRAS, 328, 89
Brown, J. M., & Millar, T. J. 2003, MNRAS, 339, 1041
Cherchneff, I., Glassgold, A. E., & Mamon, G. A. 1993, ApJ, 410, 188
Cernicharo, J., Kahane, C., Guelin, M., & Hein, H. 1987, A&A, 181, 9
Cernicharo, J., Guélin, M., Agúndez, M., Kawaguchi, K., McCarthy, M., & Thaddeus, P. 2007, A&A, 467, 37
Cernicharo, J., Guélin, M., & Kahane, C. 2000, A&AS, 142, 181
Cordiner, M. A., Millar, T. J., Walsh, C., Herbst, E., Lis, D. C., Bell, T. A., & Roueff, E. 2008, IAUS, 251, 157
Crosas, M., & Menten, K. M. 1997, ApJ, 483, 913
Dinh-V-Trung, & Lim, J. 2008, ApJ, 678, 303
Draine, B. T. 1978, ApJS, 36, 595
Dunbar, R. C., & Petrie, S. 2002, ApJ, 564, 792
Eichelberger, B., Snow, T. P., Barckholtz, C., & Bierbaum, V. M. 2007, ApJ, 667, 1283
Flower, D. R. 1999, MNRAS, 305, 651
Fonfria, J. P., Cernicharo, J., Richter, M. J., & Lacy, J. H. 2008, ApJ, 673, 445
Green, S., & Chapman, S. 1978, ApJS, 37, 169
Guélin, M., Forestini, M., Valiron, P., Ziurys, L. M., Anderson, M. A., Cernicharo, J., & Kahane, C. 1995, A&A, 297, 183
Guélin, M., Neininger, N., Lucas, R., & Cernicharo, J. 1999, in Proc. 3rd Cologne-Zermatt Symp., The Physics and Chemistry of the Interstellar Medium, ed. V. Ossenkopf (Herdecke: CGA-Verlag), 326
Gupta, H., Gottlieb, C. A., McCarthy, M. C., & Thaddeus, P. 2009, ApJ, 691, 1494
Harada, N., & Herbst, E. 2008, ApJ, 685, 272
Herbst, E., & Osamura, Y. 2008, ApJ, 679, 1670
Highberger, J. L., & Ziurys, L. M. 2003, ApJ, 597, 1065
Jura, M., & Morris, M. 1981, ApJ, 251, 189
Justtanont, K., Skinner, C. J., & Tielens, A. G. G. M. 1994, ApJ, 435, 852
Lafont, S., Lucas, R., & Omont, A. 1982, A&A, 106, 201
Lepp, S., & Dalgarno, A. 1988, ApJ, 324, 553
Lucas, R., & Guélin, M. 1999, in IAU Symp. 191, Asymptotic Giant Branch Stars, ed. T. le Bertre, A. Lebre, & C. Waelkens (San Francisco, CA: ASP), 305
Mackay, G. I., Tanaka, K., & Bohme, D. K. 1977, Int. J. Mass Spectron., 24, 125
Mauron, N., & Huggins, P. J. 2000, A&A, 359, 707
Men'shchikov, A. B., Balega, Y., Blöcker, T., Osterbart, R., & Weigelt, G. 2001, A&A, 368, 497
Millar, T. J., & Herbst, E. 1994, A&A, 288, 561
Millar, T. J., Herbst, E., & Bettens, R. P. A. 2000, MNRAS, 316, 195
Millar, T. J., Walsh, C., Cordiner, M. A., Ní Chuimín, R., & Herbst, E. 2007, ApJ, 662, L87

Nejad, L. A. M., & Millar, T. J. 1987, A&A, 183, 279
Patel, N. A., et al. 2008, A&AS, 212, 1709
Petrie, S., & Herbst, E. 1997, ApJ, 491, 210
Petrie, S., Millar, T. J., & Markwick, A. J. 2003, MNRAS, 341, 609
Prasad, S. S., & Huntress, W. T., Jr. 1980, ApJS, 43, 1
Remijan, A. J., Hollis, J. M., Lovas, F. J., Cordiner, M. A., Millar, T. J., Markwick-Kemper, A. J., & Jewell, P. R. 2007, ApJ, 664, L47
Tarroni, R., & Carter, S. 2004, Mol. Phys., 102, 21, 2167
Thaddeus, P., Gottlieb, C. A., Gupta, H., Brünken, S., McCarthy, M. C., Agúndez, M., Guélin, M., & Cernicharo, J. 2008, ApJ, 677, 1132
Truong-Bach, Morris, D., & Nguyen-Q-Rieu, 1991, A&A, 249, 435
Woodall, J., Agúndez, M., Markwick-Kemper, A. J., & Millar, T. J. 2007, A&A, 466, 1197
Woon, D. E. 1995, Chem. Phys. Lett., 244, 45
Ziurys, L. M., Savage, C., Highberger, J. L., Apponi, A. J., Guélin, M., & Cernicharo, J. 2002, ApJ, 564, L45